Int. J. Solids Structures Vol. 30, No. 21, pp. 2879–2893, 1993
Printed in Great Britain

0020–7683/93 $6.00+ .00

AN ANALYSIS OF LOW-VELOCITY IMPACT OF SPHERES ON ELASTIC CURVED-SHELL STRUCTURES

DAE ILL LEE and BYUNG MAN KWAK
Department of Mechanical Engineering, The Korea Advanced Institute of Science and Technology, 373-1 Kuseong-dong, Yuseong-ku, Taejon, 305-701, Korea

(*Received* 17 *February* 1993; *in revised form* 27 *April* 1993)

Abstract—A solution method for dynamic analysis of low-velocity impact between elastic curved-shell structures and spheres is presented. The discretized nonlinear impact equations are derived based on the degenerated shell FE formulation and the Hertzian contact theory. They are numerically integrated to get various transient responses such as contact force and other field quantities. The validity and applicability of the method are shown numerically with two model problems of practical importance.

INTRODUCTION

For safety evaluation and design of structures under impact, it is important to know local dynamic responses (Johnson, 1972; Zukas, 1982). Timoshenko (1913) applied the Hertzian contact theory to analyse the low-velocity impact problem between a beam and a steel ball. In his study, impact phenomenon was described by a simple one degree-of-freedom model. This model gives a good approximation when applied to the impact between bodies like spheres. It has also been proved to be highly applicable to target structures such as beam, plate and shell structures through theoretical and experimental studies (Chen and Engel, 1972; Koller and Busenhart, 1986; Ujihashi *et al.*, 1986; Mittal, 1987; Jingu *et al.*, 1987). In another approach, the history of contact force is assumed to be known as an external impulse (Eringen, 1950; Sankar and Sun, 1985; Ramkumar and Thakar, 1987). Sometimes it is obtained by impact experiments (Kunukkasseril and Palaninathan, 1975; Barez and Goldsmith, 1981). Although Lee *et al.* (1983) presented a lumped parameter method, they have difficulty in determining the so-called transfer mobility, whose value is critical for the simulation of the impact phenomenon. Various simplifications were also proposed (Shivakumar *et al.*, 1985; Schonberg *et al.*, 1987).

In earlier models, shells of simple geometrical shapes (exponential, conic, spherical shell and so on) were treated adopting transformation techniques to obtain the transient responses (Engin, 1969; Kenner and Goldsmith, 1972; Kunukkasseril and Palaninathan, 1975). Hammel (1976) analysed the elastic spherical shell impact problem with a simplified model using springs and dash-pots. Koller and Busenhart (1986) solved an impact problem between a shallow spherical glass shell and a steel sphere using Reissner's approximate theory and Hertzian contact theory, and compared their results with experiments. However, their formulation could not describe the behavior of reflexive waves from the boundaries of the spherical shell.

In the present paper, a solution method for the dynamic analysis of low-velocity impact between a curved-shell structure and a sphere is presented. The degenerated shell finite elements are used for modeling the target structure, and the impact phenomenon is described by a one degree-of-freedom model based on Hertzian contact theory. The discretized nonlinear impact equations are numerically integrated to get the transient response using the Adams predictor–corrector method. Two numerical examples are studied to show the validity and applicability of the method. A simulation of the impact of a sphere on a television bulb has been in mind.

THE DEGENERATED SHELL FINITE ELEMENTS OF ELASTIC CURVED-SHELL STRUCTURES

To derive dynamic equations of motion of a curved-shell structure, the degeneration formulation (Ahmad *et al.*, 1970) is used, where the three-dimensional equations of continuum mechanics are directly discretized. Improvements for both thin and thick shells have been possible (Zienkiewicz *et al.*, 1971; Pawsey and Clough, 1971).

Two assumptions are used in this formulation. Firstly, it is assumed that the normal to the middle surface of the shell element remains straight allowing loss of normality after deformation. Secondly, the strain energy corresponding to stresses perpendicular to the middle surface is ignored, i.e. the stress component normal to the middle surface is zero.

Four different coordinate systems, i.e. global, nodal, curvilinear and local coordinate systems, are adopted in the geometry identification and deformation kinematics of degenerated shell finite elements (Hinton and Owen, 1984), as shown in Fig. 1.

Using the isoparametric formulation, the coordinates of a point within an element are determined by element shape functions and nodal coordinates on the middle surface as follows:

$$\begin{Bmatrix} x \\ y \\ z \end{Bmatrix} = \sum_{k=1}^{n} N_k(\xi,\eta) \begin{Bmatrix} x_k \\ y_k \\ z_k \end{Bmatrix}_{\text{mid}} + \sum_{k=1}^{n} N_k(\xi,\eta)\zeta \frac{h_k}{2} \begin{Bmatrix} \bar{\mathbf{v}}_{3k}^{x} \\ \bar{\mathbf{v}}_{3k}^{y} \\ \bar{\mathbf{v}}_{3k}^{z} \end{Bmatrix}, \tag{1}$$

where n is the number of nodes of an element, $N_k(\xi,\eta)$ is the element shape function corresponding to the surface ζ = constant, h_k is the thickness of the shell at the kth node, i.e. the respective normal length, and ξ, η and ζ are the curvilinear coordinates of the point under consideration. The vector $\mathbf{v}_{3k}$ is determined by $\mathbf{v}_{3k} = \mathbf{x}_k^{\text{top}} - \mathbf{x}_k^{\text{bot}}$, where $\mathbf{x}_k = \{x_k, y_k, z_k\}^{\mathrm{T}}$. The $\bar{\mathbf{v}}_{3k}$ denotes the unit vector of $\mathbf{v}_{3k}$, and its direction cosines with respect to the global coordinate system are denoted by $\bar{\mathbf{v}}_{3k}^{j}$ $(j = x, y, z)$.

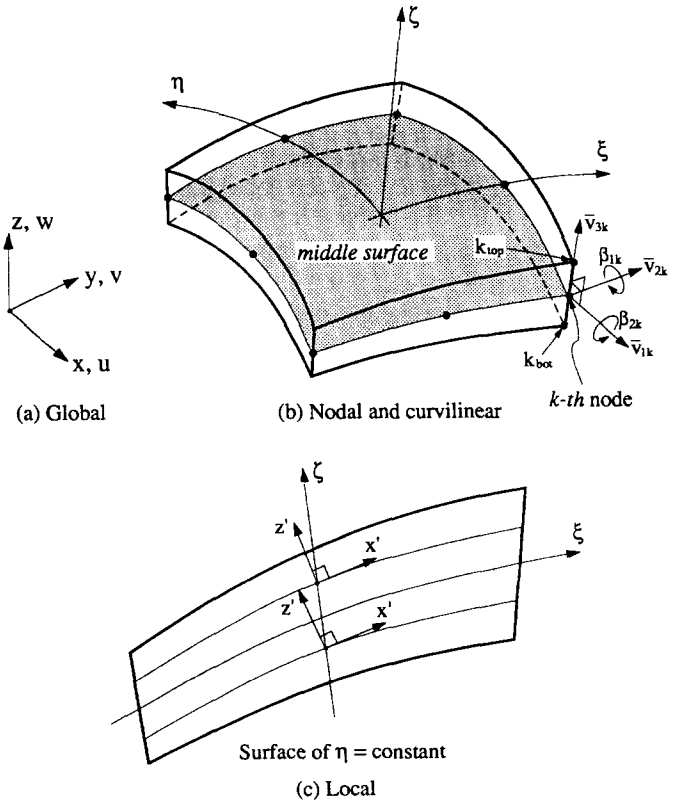

Fig. 1. Four coordinate systems used in the degenerated shell formulation.

The displacement field in a degenerated shell element is defined by the three translational displacements of its mid-point and two rotational displacements of a normal at every node. The definition of independent translational and rotational degrees of freedom permits transverse shear deformation to be taken into account, since rotations are independent of the slope of the middle surface. Thus

$$\begin{Bmatrix} u \\ v \\ w \end{Bmatrix} = \sum_{k=1}^{n} N_k(\xi,\eta) \begin{Bmatrix} u_k \\ v_k \\ w_k \end{Bmatrix}_{\text{mid}} + \sum_{k=1}^{n} N_k(\xi,\eta)\zeta \frac{h_k}{2} \begin{bmatrix} \bar{\mathbf{v}}_{1k}^x & \bar{\mathbf{v}}_{2k}^x \\ \bar{\mathbf{v}}_{1k}^y & \bar{\mathbf{v}}_{2k}^y \\ \bar{\mathbf{v}}_{1k}^z & \bar{\mathbf{v}}_{2k}^z \end{bmatrix} \begin{Bmatrix} \beta_{1k} \\ \beta_{2k} \end{Bmatrix}, \tag{2}$$

where u_k, v_k and w_k are the nodal translational displacements and β_{1k} and β_{2k} the rotational displacements at the kth node in an element (Fig. 1). The $\bar{\mathbf{v}}_{ik}^j$ $(j = x, y, z)$ denote the direction cosines of the $\bar{\mathbf{v}}_{ik}$ $(i = 1, 2)$ with respect to the global coordinate system, and the $\bar{\mathbf{v}}_{ik}$ denote the unit vectors of $\mathbf{v}_{ik}$. Again, the nodal displacement vector at the kth node is defined as

$$\mathbf{q}_k^{\mathrm{t}} = \{u_k, v_k, w_k, \beta_{1k}, \beta_{2k}\}^{\mathrm{T}}, \tag{3}$$

where the superscript 't' means the target body.

Then, the element displacement and acceleration fields for a complete element can be written as

$$\mathbf{u} \cong \mathbf{N}\mathbf{q}_{\mathrm{e}}^{\mathrm{t}},$$

and

$$\ddot{\mathbf{u}} \cong \mathbf{N}\ddot{\mathbf{q}}_{\mathrm{e}}^{\mathrm{t}}, \tag{4}$$

where $\mathbf{u} = \{u, v, w\}^{\mathrm{T}}$ is the element displacement vector, $\mathbf{N} = [\mathbf{N}_1, \ldots, \mathbf{N}_k, \ldots, \mathbf{N}_n]$ the element shape-function matrix, and $\mathbf{q}_{\mathrm{e}}^{\mathrm{t}} = \{\mathbf{q}_1^{\mathrm{t}^{\mathrm{T}}}, \ldots, \mathbf{q}_k^{\mathrm{t}^{\mathrm{T}}}, \ldots, \mathbf{q}_n^{\mathrm{t}^{\mathrm{T}}}\}^{\mathrm{T}}$ an element nodal displacement vector. The explicit form of $\mathbf{N}_k$ is described in the Appendix.

The local coordinate system is convenient to treat the assumption of zero normal stress in the z'-direction, i.e. $\sigma_{z'} = 0$. Thus the five significant strain components have the following relation with the displacements expressed by the local coordinate system, i.e.

$$\varepsilon = \begin{Bmatrix} \varepsilon_{x'} \\ \varepsilon_{y'} \\ \gamma_{x'y'} \\ \gamma_{x'z'} \\ \gamma_{y'z'} \end{Bmatrix} = \begin{Bmatrix} \dfrac{\partial u'}{\partial x'} \\ \dfrac{\partial v'}{\partial y'} \\ \dfrac{\partial u'}{\partial y'} + \dfrac{\partial v'}{\partial x'} \\ \dfrac{\partial u'}{\partial z'} + \dfrac{\partial w'}{\partial x'} \\ \dfrac{\partial v'}{\partial z'} + \dfrac{\partial w'}{\partial y'} \end{Bmatrix}. \tag{5}$$

By differentiation,

$$\boldsymbol{\varepsilon} = \mathbf{B}\mathbf{q}_{\mathrm{e}}^{\mathrm{t}}, \tag{6}$$

where $\mathbf{B}$ denotes the element strain matrix (Weaver and Johnston, 1987).

The corresponding five stress components under the local coordinates system are defined as

$$\boldsymbol{\sigma} = \{\sigma_{x'}, \sigma_{y'}, \tau_{x'y'}, \tau_{x'z'}, \tau_{y'z'}\}^{\mathrm{T}}, \tag{7}$$

and the constitutive relation, i.e. Hooke's law, for isotropic and homogeneous materials is

$$\boldsymbol{\sigma} = \mathbf{D}\boldsymbol{\varepsilon}, \tag{8}$$

where $\mathbf{D}$ is the elastic matrix given by

$$\mathbf{D} = \begin{bmatrix} D_1 & D_{12} & 0 & 0 & 0 \\ & D_2 & 0 & 0 & 0 \\ & & D_3 & 0 & 0 \\ & \text{symm.} & & D_4 & 0 \\ & & & & D_5 \end{bmatrix}, \tag{9}$$

where $D_1 = D_2 = E_t/(1-\nu_t^2)$, $D_{12} = E_t\nu_t/(1-\nu_t^2)$, $D_3 = E_t/2(1+\nu_t)$ and $D_4 = D_5 = E_t/2\kappa(1+\nu_t)$, with E_t, ν_t and κ being the Young's modulus, Poisson's ratio and shear correction factor, respectively. The shear correction factor κ is taken to be 1.2 which is calculated based on the transverse shear strain energy on an average basis (Ahmad *et al.*, 1970).

By introducing the layered approach (Hinton, 1984), the actual stress distribution of the shell is modeled by a piecewise constant approximation over the thickness. The stress points are located on the mid-surface of each layer.

Applying the formal procedure of FEM based on the aforementioned displacement, acceleration, strain and stress fields, the global consistent mass matrix $\mathbf{M}^t$ (Weaver and Johnston, 1987) and the stiffness matrix $\mathbf{K}^t$ can be obtained as

$$\mathbf{M}^t = \sum_e \int_{-1}^{+1}\int_{-1}^{+1}\int_{-1}^{+1} \rho \mathbf{N}^T\mathbf{N}|\mathbf{J}|\,d\xi\,d\eta\,d\zeta$$

and

$$\mathbf{K}^t = \sum_e \int_{-1}^{+1}\int_{-1}^{+1}\int_{-1}^{+1} \mathbf{B}^T\mathbf{D}\mathbf{B}|\mathbf{J}|\,d\xi\,d\eta\,d\zeta, \tag{10}$$

where ρ denotes the density of the shell and $|\mathbf{J}|$ is the determinant of the Jacobian matrix. The global applied force vector induced by impact can be described by using the Hertzian contact theory.

DERIVATION OF DISCRETIZED IMPACT EQUATIONS BASED ON THE HERTZIAN CONTACT THEORY

The response induced by the low-velocity impact of a sphere can be described using the Hertzian contact theory with a good approximation in the frictionless case. According to this theory, the unknown contact force f_c during the impact is given as

$$f_c = h\alpha^{3/2}, \tag{11}$$

where α denotes the elastic approach defined as $\alpha = q^{ic} - q^{tc}$. Here, q^{ic} and q^{tc} are taken as the displacements of the impactor and the target along the z-direction, as defined in Fig. 2. And h is the Hertzian constant which is determined by the material and geometrical constants of the impactor and target as follows:

$$h = \sqrt{\frac{8}{\beta}}\frac{E_r}{3\pi}, \tag{12}$$

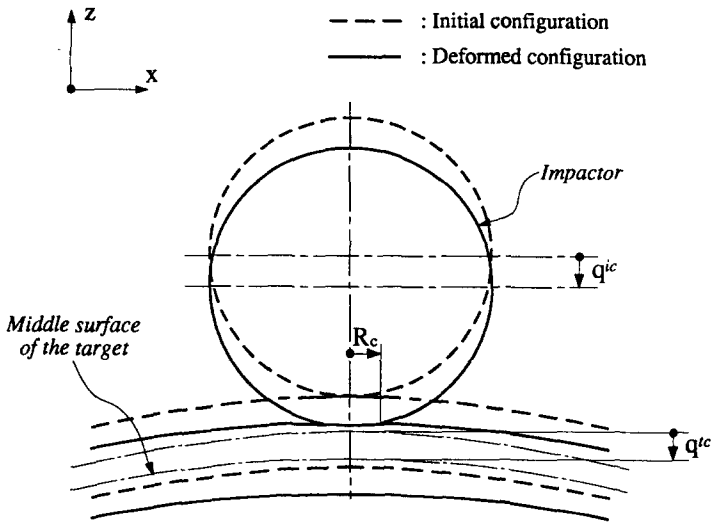

Fig. 2. Kinematic configuration of the Hertzian contact model.

where the combined curvature β and the reduced modulus E_r are given by

$$\beta = \frac{1}{2}\left(\frac{1}{R_i} + \frac{1}{R_t}\right), \tag{13}$$

$$E_r = \left(\frac{1-\nu_i^2}{\pi E_i} + \frac{1-\nu_t^2}{\pi E_t}\right)^{-1}. \tag{14}$$

Here R_i, E_i and ν_i are the radius of curvature, Young's modulus and Poisson's ratio of the impactor, respectively, and R_t is the radius of curvature of the target.

The histories of contact radius R_c and maximum contact pressure P_m can be calculated from the following relations:

$$R_c = \sqrt{\frac{\alpha}{2\beta}}$$

and

$$P_m = \frac{\sqrt{2\beta E_r}}{\pi^2}\alpha^{1/2}. \tag{15}$$

Using this one degree-of-freedom contact model, the global nodal force vector applied to the target can be expressed as

$$\mathbf{F}^t = -f_c\mathbf{e} = -h\alpha^{3/2}\mathbf{e}, \tag{16}$$

where $\mathbf{e}$ is a vector, whose only nonzero component corresponding to the global d.o.f. of q^{tc} is unity. The other components are all zero.

By considering eqns (10)–(14) and (16), the discretized nonlinear impact equations are obtained as follows:

$$\begin{aligned} \mathbf{M}^t\ddot{\mathbf{q}}^t + \mathbf{C}^t\dot{\mathbf{q}}^t + \mathbf{K}^t\mathbf{q}^t &= \mathbf{F}^t, \\ m^i\ddot{q}^{ic} &= f_c, \end{aligned} \tag{17}$$

where the damping matrix $\mathbf{C}^t$ may be appropriately introduced depending on application cases. And m^i denotes the mass of the impacting sphere.

By defining

$$\mathbf{q} = \begin{Bmatrix} \mathbf{q}^t \\ q^{ic} \end{Bmatrix},$$

$$\mathbf{M} = \begin{bmatrix} \mathbf{M}^t & \mathbf{0} \\ \mathbf{0}^T & m^i \end{bmatrix},$$

$$\mathbf{C} = \begin{bmatrix} \mathbf{C}^t & \mathbf{0} \\ \mathbf{0}^T & 0 \end{bmatrix},$$

$$\mathbf{K} = \begin{bmatrix} \mathbf{K}^t & \mathbf{0} \\ \mathbf{0}^T & 0 \end{bmatrix},$$

$$\mathbf{F} = \begin{Bmatrix} \mathbf{F}^t \\ f_c \end{Bmatrix}, \tag{18}$$

eqn (17) can be rewritten as

$$\mathbf{M}\ddot{\mathbf{q}} + \mathbf{C}\dot{\mathbf{q}} + \mathbf{K}\mathbf{q} = \mathbf{F}. \tag{19}$$

For numerical time integration, eqn (19) is changed to a system of first-order equations by introducing auxiliary variables $\mathbf{x}_1$ and $\mathbf{x}_2$ as follows:

$$\mathbf{x}_1 = \mathbf{q},$$
$$\mathbf{x}_2 = \dot{\mathbf{q}}. \tag{20}$$

Thus one has

$$\mathbf{M}^a\dot{\mathbf{x}} + \mathbf{K}^a\mathbf{x} - \mathbf{F}^a = \mathbf{0}, \tag{21}$$

where $\mathbf{x}$, $\mathbf{M}^a$, $\mathbf{K}^a$ and $\mathbf{F}^a$ are given by

$$\mathbf{x} = \begin{Bmatrix} \mathbf{x}_1 \\ \mathbf{x}_2 \end{Bmatrix},$$

$$\mathbf{M}^a = \begin{bmatrix} \mathbf{I} & \mathbf{0} \\ \mathbf{0} & \mathbf{M} \end{bmatrix},$$

$$\mathbf{K}^a = \begin{bmatrix} \mathbf{0} & -\mathbf{I} \\ \mathbf{K} & \mathbf{C} \end{bmatrix}$$

and

$$\mathbf{F}^a = \begin{Bmatrix} \mathbf{0} \\ \mathbf{F} \end{Bmatrix}. \tag{22}$$

Here $\mathbf{x}$ denotes the augmented state-variable vector, $\mathbf{M}^a$ the augmented mass matrix, $\mathbf{K}^a$ the augmented stiffness matrix and $\mathbf{F}^a$ the augmented applied force vector. It is noted that the augmented mass matrix is symmetric, but the augmented stiffness matrix is not.

This augmented impact equation is solved numerically using the Adams predictor-corrector method (IMSL, 1984), which adopts a variable time-step strategy. The detailed computational procedure of the developed computer program is in Fig. 3.

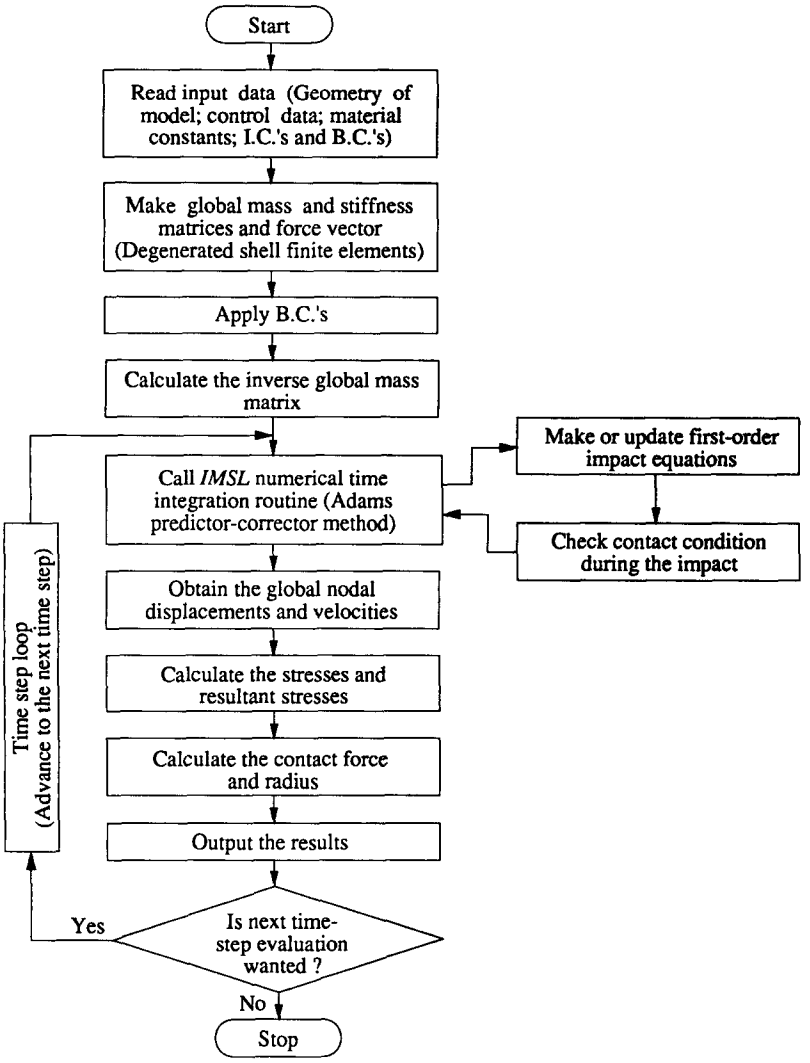

Fig. 3. Flow chart of the computer program.

NUMERICAL EXAMPLES AND DISCUSSIONS

Two numerical examples without damping are prepared to demonstrate the capability and applicability of the proposed formulation. A quadratic interpolation is used, and related shape functions and nodal shape function matrix are described in Appendix. The number of layers over the shell's thickness is four.

Example 1. Impact between a glass plate and a steel sphere

A square glass plate which is impacted by a steel sphere is taken to show the validity and performance of the present formulation. The details of the geometrical configuration

Table 1. Material properties used for the analysis of numerical examples

	Materials	
Properties	Glass (plate or cap)	Steel (sphere)
Young's modulus (GPa)	69.65	206.0
Shear modulus (GPa)	28.31	79.85
Density (kg m^{-3})	2,492	7,833
Poisson's ratio	0.23	0.29

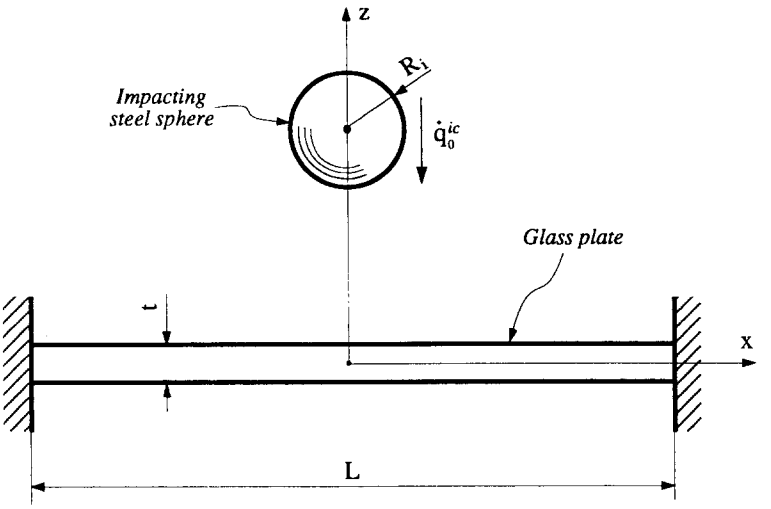

Fig. 4. Geometrical configuration of the impact model of example 1.

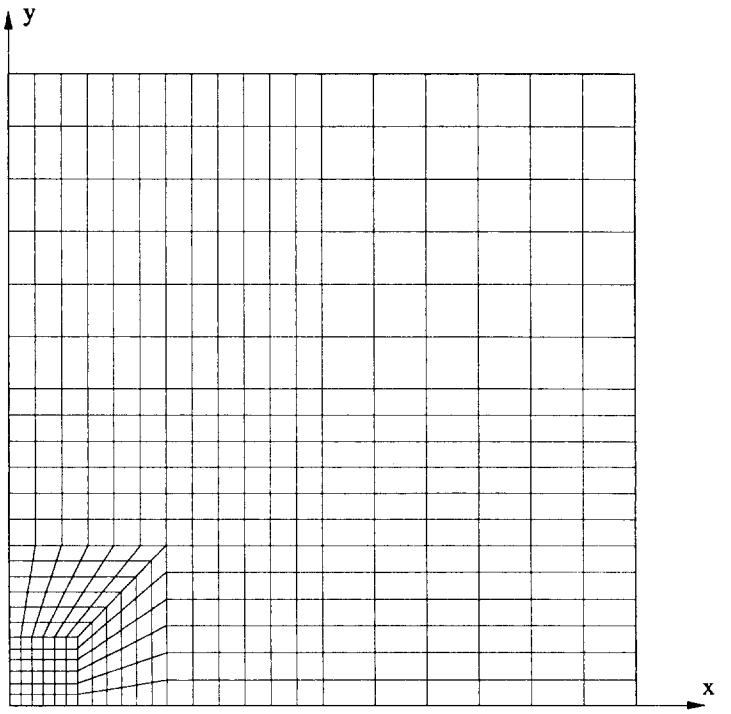

Fig. 5. Finite element mesh of the plate on the plane $z = 0$, example 1.

of this impact model is depicted in Fig. 4. The dimensions of the glass plate are $L \times L \times t = 600 \times 600 \times 6$ mm and, because of symmetry, the finite element model of the plate is taken as in Fig. 5. It consists of 396 elements and 1273 nodes and the periphery of the plate is fixed. The material properties for numerical computation are given in Table 1. Three cases of impact conditions are considered in this example, as summarized in Table 2.

Table 2. Three cases of the impact conditions and related parameters for plate impact analysis

	R_i (mm)	$\dot{q}_0^{ic}$ (m s^{-1})	λ	β'
Case 1	8.80	3.288	1.0	0.05
Case 2	32.43	0.714	10.0	0.01
Case 3	31.75	4.603	13.92	0.015

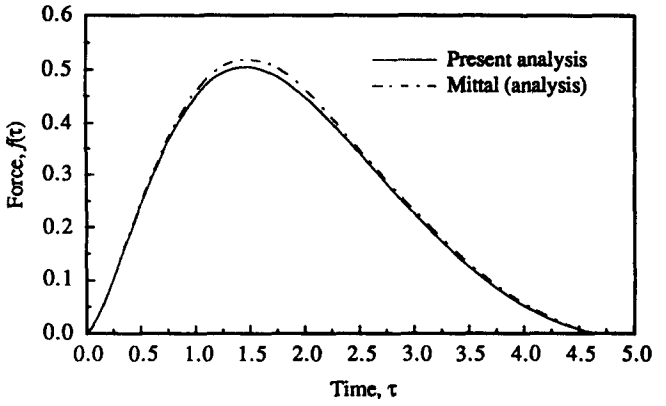

(a) $\lambda = 1.0$ and $\beta' = 0.05$

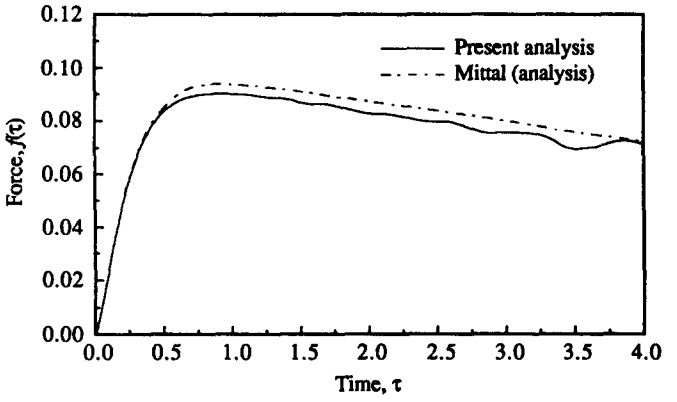

(b) $\lambda = 10.0$ and $\beta' = 0.01$

Fig. 6. Comparison of the contact force histories with different impact and shear parameters.

Cases 1 and 2 are prepared to show the validity of the present solution method through comparing the results by the analytical method of Mittal (1987). Mittal introduced an impact parameter, $\lambda = (\alpha_p m^{i}/T_0)$, and a shear parameter, $\beta' = (9.6\rho\lambda D/m^{i}G_t)$, in dimensionless forms, where $T_0 = (m^{i^{2/5}}/h^{2/5}\dot{q}_0^{ic^{1/5}})$, $\alpha_p = (1/8\sqrt{\rho t D})$, $D = (E_t t^3/12(1-\nu_t^2))$ and G_t denote the reference time, plate parameter, flexural rigidity of plate and transverse shear modulus, respectively. The values taken for the two cases are given in Table 2.

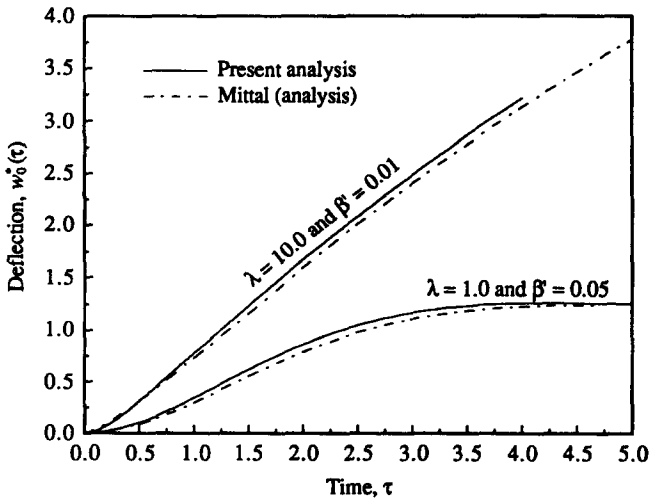

Fig. 7. Comparison of the deflection histories at impact point of the glass plate with different impact and shear parameters.

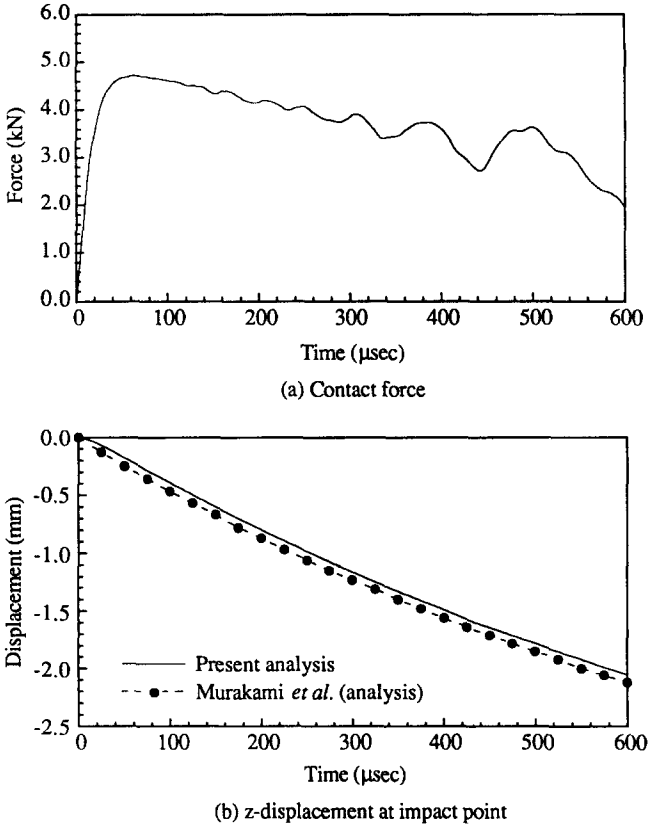

Fig. 8. Time histories of the contact force and z-displacement at impact point.

A nondimensional force, $f(\tau) = (T_0/m^i\dot{q}_0^{ic})f_c(t)$, and deflection at the point of impact, $w_0^*(\tau) = (1/T_0\dot{q}_0^{ic})w_0(t)$, are obtained with respect to the nondimensional time, $\tau = (t/T_0)$, as in Figs 6 and 7, respectively. The two results of the present and Mittal's analyses coincide well with each other. It is noted in Fig. 6(b) that the contact force by the present analysis starts to oscillate around $\tau = 1.5$. That happens because the reflexive flexural waves from the fixed boundary of the plate arrive at the point of impact and affect the contact force thereafter.

The problem under the impact condition of case 3 is analysed, where the analysis time taken in 600 μs considering the huge computational work. The time histories of the contact force and displacement at impact point are obtained as in Fig. 8. It is seen that the contact duration becomes very long and the effect of reflexive waves on it is considerable with this large value of $\lambda = 13.92$. The time history of the displacement is compared with the results reconstructed manually from the paper published at Murakami *et al.* (1990), and show relatively good agreement.

The radial and circumferential stress histories at check point "1" ($x = y = 0$ and $z = -3$ mm) and "2" ($x = 100$, $y = 0$ and $z = -3$ mm) on the bottom surface of the plate are plotted in Fig. 9. There is considerable difference in the radial stress at check point "1", although the results for check point "2" agree well with Murakami's. The arrival time of the stress wave at check point "2" is about 18 μs, which nearly coincides with the value of 19.2 μs calculated with the longitudinal wave velocity 5,203 m s^{-1} of the glass.

Example 2. Impact between a spherical glass cap and a steel sphere

A spherical glass cap which is impacted by a steel sphere is taken to show the applicability of the method to curved-shell structures. The details of the geometrical configuration of the impact model are depicted in Fig. 10. The periphery of the spherical cap is fixed. The radius of the impacting sphere, R_i, is 3 mm and impact velocity of the sphere, $\dot{q}_0^{ic}$, is 1.3 m s^{-1}. The radius of curvature, R_t, the base diameter, D, and the thickness of the glass

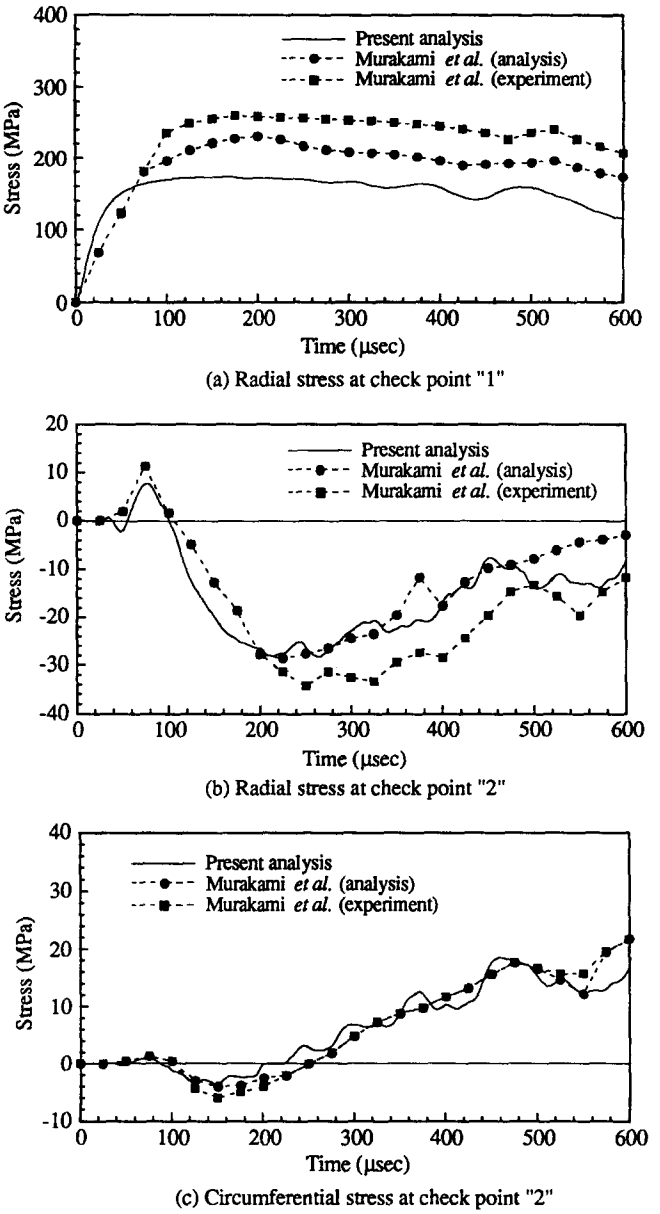

Fig. 9. Time histories of the radial and circumferential stresses on the bottom surface.

spherical cap, t, are 330, 200 and 1.9 mm, respectively. Due to symmetry, a quarter of the spherical cap is taken and depicted in Fig. 11. It consists of 100 elements and 351 nodes and the material properties are the same as those of example 1.

The time history of the contact force and the vertical displacement at the impact point of the spherical cap are obtained as in Fig. 12 and compared with those by Koller *et al.* (1986). The contact duration is calculated as 37 μs after impact. Although exact comparison is not possible since Koller *et al.* did not identify the material properties used in their paper, the overall behavior exhibits good agreement during the analysis period.

The radial and effective stress histories at two check points on the bottom surface of the spherical cap are presented in Fig. 13. Check point "1", the first Gaussian point of the first element, is near the impact point and check point "2" is the second Gaussian point of the 53rd element as illustrated in Fig. 11. It is confirmed that low-velocity impact phenomenon is well simulated with this finite element model using the present formulation.

Next we investigated the effects of the impact velocity and the radius of the impacting sphere on the contact force. Figure 14 shows that the maximum contact force is increased

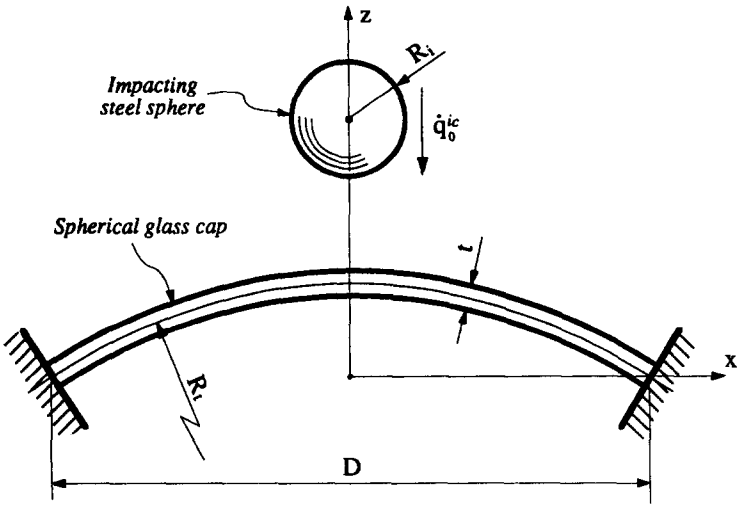

Fig. 10. Geometrical configuration of the impact model of example 2.

as the mass of the sphere becomes heavier. Especially, it is observed that the second and third contacts are occurring at 134 and 179 μs, respectively, in the case of $R_i = 4$ mm. The case of $R_i = 3.5$ mm exhibits a similar multiple impact. The maximum contact force increases noticeably as the impact velocity of the sphere becomes higher. However, the contact duration does not change considerably. The variation of the maximal radial stress at check point "1" with respect to the change of the impact condition is given in Table 3. The stress increases and levels horizontally as the size of impacting ball increases. However, it is almost linearly proportional to the initial velocity.

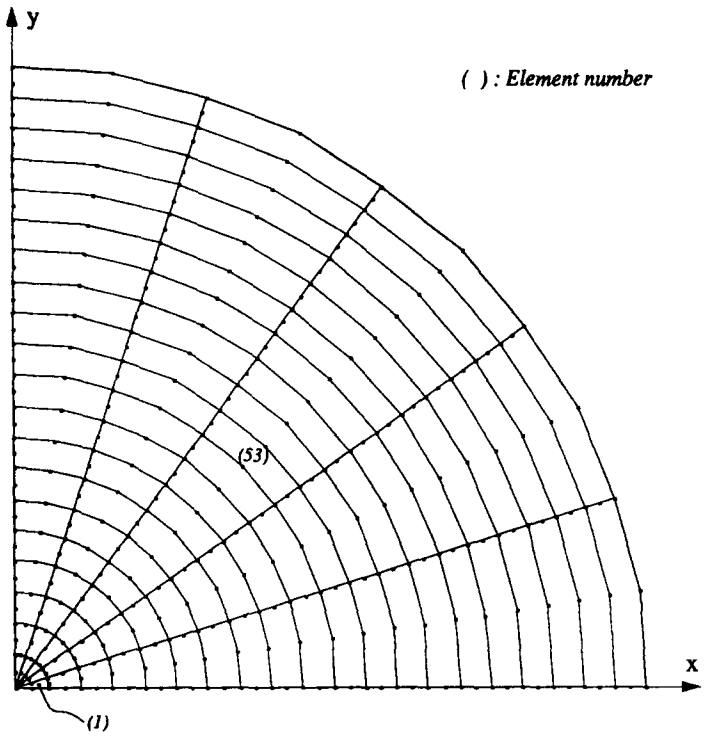

Fig. 11. Finite element mesh of the spherical glass cap on the plane $z = 0$, example 2.

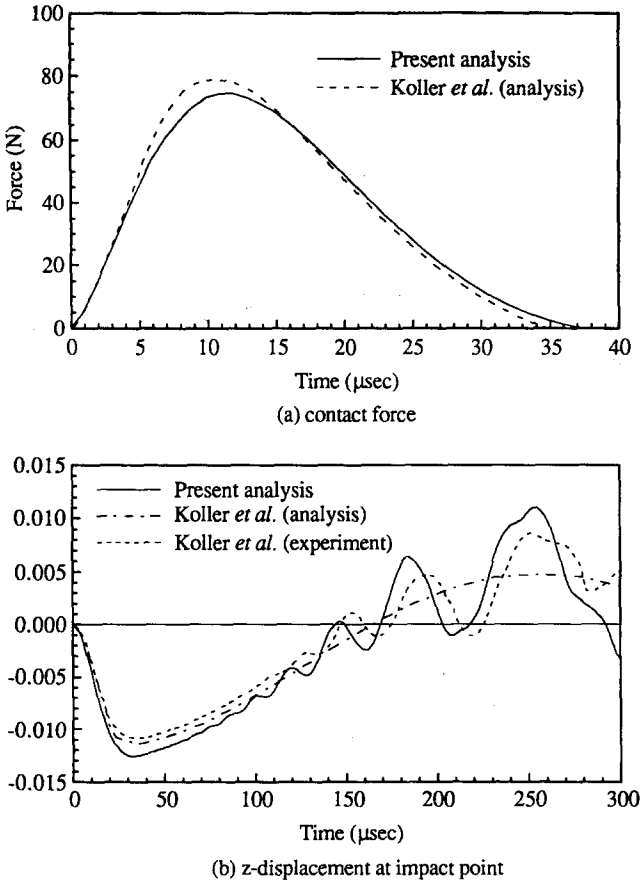

Fig. 12. Time histories of the contact force and z-displacement at impact point.

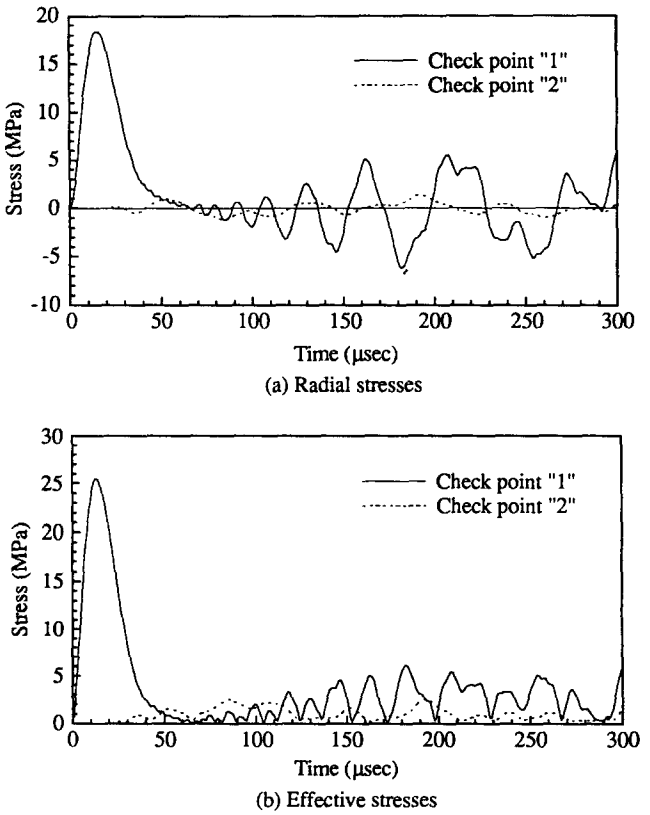

Fig. 13. Time histories of the radial and effective stresses on the bottom surface.

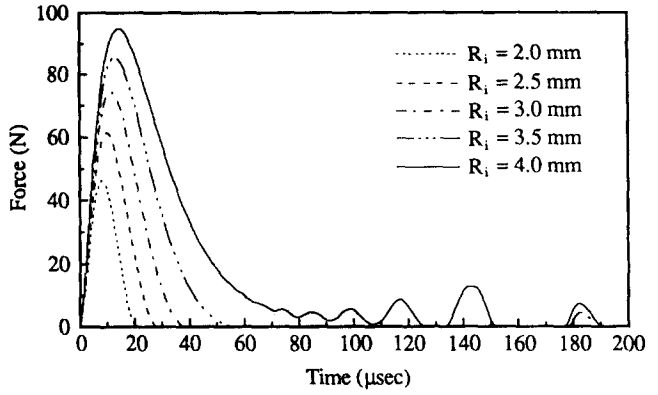

(a) Effect of radius of sphere, $\dot{q}_0^{ic}$ = 1.3 m/sec

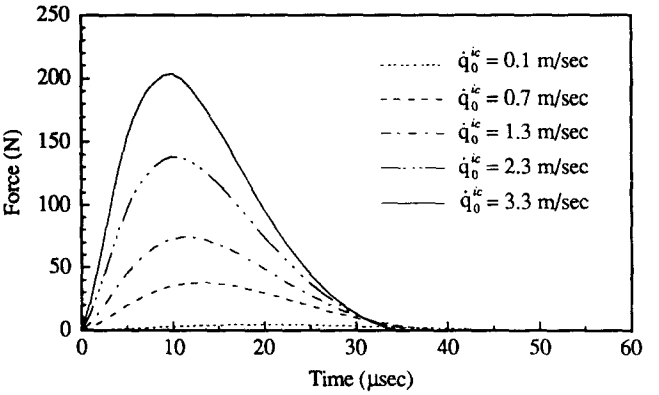

(b) Effect of impact velocity, R_i = 3.0 mm

Fig. 14. Time histories of the contact force with respect to the change of impact condition.

Table 3. Variation of the maximum radial stress, σ^r_{max}, and the time when it occurs, t^0, with the change of impact condition

$\dot{q}_0^{ic}$ = 1.3 m s^{-1}			R_i = 3 mm		
R_i (mm)	σ^r_{max} (MPa)	t^0 (μs)	$\dot{q}_0^{ic}$ (m s^{-1})	σ^r_{max} (MPa)	t^0 (μs)
2.0	10.40	11.0	0.1	1.20	24.0
2.5	14.66	12.0	0.7	9.61	17.0
3.0	18.43	15.0	1.3	18.43	15.0
3.5	21.87	17.0	2.3	33.54	14.0
4.0	24.90	19.0	3.3	48.93	13.0

CONCLUSIONS

A solution method for dynamic analysis of low-velocity impact between elastic curved-shell structures and spheres is presented. The discretized nonlinear impact equations are derived based on the degenerated shell finite elements and the Hertzian contact theory. The method can calculate the unknown contact force and other histories during the impact.

It is shown to be applicable to plate and spherical cap impact problems. The results are favorably compared with those of existing literature. In addition, it is capable of describing wave propagations and can be used for practical purposes with refined meshes.

Acknowledgement—The authors gratefully acknowledge the financial support of Samsung Corning Co., Ltd.

REFERENCES

Ahmad, S. B., Irons, M. and Zienkiewicz, O. C. (1970). Analysis of thick and thin shell structures by curved finite elements. *Int. J. Num. Meth. Engng* **2,** 419–451.

Barez, F. and Goldsmith, W. (1981). Pulse transmission in elastic exponential and conical shells. *Int. J. Mech. Sci.* **23,** 661–675.

Chen, W. T. and Engel, P. A. (1972). Impact and contact stress analysis in multilayer media. *Int. J. Solids Structures* **8,** 1257–1281.

Engin, A. E. (1969). The axisymmetric response of a fluid-filled spherical shell to a local radial impulse—a model for head injury. *J. Biomech.* **2,** 325–341.

Eringen, A. C. (1950). Transverse impact on beams and plates. *ASME J. Appl. Mech.* **72,** 461–468.

Hammel, J. (1976). Aircraft impact on a spherical shell. *Nucl. Engng Des.* **37,** 205–223.

Hinton, E. and Owen, D. R. J. (1984). *Finite Element Software for Plates and Shells.* Pineridge Press, Swansea.

IMSL (1984). *IMSL Library: Problem-Solving Software System for Mathematical and Statistical FORTRAN Programming—User's Manual.* IMSL, U.S.A.

Jingu, T., Matsumoto, H., Nezu, K. and Sakamoto, K. (1987). The effect of local contact behavior on an impact load due to collision between a plate and a sphere. *JSME(A)* **53,** 2331–2335.

Johnson, W. (1972). *Impact Strength of Materials.* Edward Arnold, London.

Kenner, V. H. and Goldsmith, W. (1972). Dynamic loading of a fluid-filled spherical shell. *Int. J. Mech. Sci.* **14,** 557–568.

Koller, M. G. and Busenhart, M. (1986). Elastic impact of spheres on thin shallow spherical shells. *Int. J. Impact Engng* **4,** 11–21.

Kunukkasseril, V. X. and Palaninathan, R. (1975). Impact experiments on shallow spherical shells. *J. Sound Vibr.* **40,** 101–117.

Lee, Y., Hamilton, J. F. and Sullivan, J. W. (1983). Lumped parameter method for elastic impact problems. *Trans. ASME J. Appl. Mech.* **50,** 823–827.

Mittal, R. K. (1987). A simplified analysis of the effect of transverse shear on the response of elastic plates to impact loading. *Int. J. Solids Structures* **23,** 1191–1203.

Murakami, T., Nishihama, J., Matsumoto, T. and Sato, Y. (1990). Impact simulation of architectural glass by means of finite element method. *Reports Res. Lab. Asahi Glass Co., Ltd.* **40,** 1–13.

Pawsey, S. E. and Clough, R. W. (1971). Improved numerical integration of thick shell finite elements, *Int. J. Num. Meth. Engng* **3,** 575–586.

Ramkumar, R. L. and Thakar, Y. R. (1987). Dynamic response of curved laminated plates subjected to low velocity impact. *Trans. ASME J. Engng Mater. Tech.* **109,** 67–71.

Sankar, B. V. and Sun, C. T. (1985). An efficient numerical algorithm for transverse impact problems. *Comput. Struct.* **20,** 1009–1012.

Schonberg, W. P., Keer, L. M. and Woo, T. K. (1987). Low-velocity impact of transversely isotropic beams and plates. *Int. J. Solids Structures* **23,** 871–896.

Shivakumar, K. N., Elber, W. and Illg, W. (1985). Prediction of impact force and duration due to low-velocity impact on circular composite laminates. *Trans. ASME J. Appl. Mech.* **52,** 674–680.

Timoshenko, S. P. (1913). Zur Frage nach der Wirkung eines Stoßes auf einen Balken. *Z. Math. Phys.* **62,** 198–209.

Ujihashi, S., Adachi, T., Inoue, H. and Matsumoto, H. (1986). An analytical and experimental study of impulsive stresses in a glass plate subjected to the transverse impact of steel balls. *JSME(A)* **52,** 525–532.

Weaver, W., Jr and Johnston, P. R. (1987). *Structural Dynamics by Finite Elements.* Prentice-Hall, New Jersey.

Zienkiewicz, O. C., Taylor, R. L. and Too, J. M. (1971). Reduced integration technique in general analysis of plates and shells. *Int. J. Num. Meth. Engng* **3,** 275–290.

Zukas, J. A. (1982). *Impact Dynamics.* A Wiley-Interscience Publication, New York.

APPENDIX: SHAPE FUNCTIONS USED

Eight quadratic shape functions are:

$$\begin{aligned} N_k &= \tfrac{1}{4}(1+\xi_0)(1+\eta_0)(-1+\xi_0+\eta_0), && k=1,2,3,4,\\ N_k &= \tfrac{1}{2}(1-\xi^2)(1+\eta_0), && k=5,7,\\ N_k &= \tfrac{1}{2}(1+\xi_0)(1-\eta^2), && k=6,8, \end{aligned} \tag{A1}$$

where $\xi_0 = \xi_k\xi$ and $\eta_0 = \eta_k\eta$. The ξ_k and η_k denote the values of the ξ and η at the kth node in an element, respectively.

Nodal shape function matrix at the kth node is:

$$\mathbf{N}_k = \begin{bmatrix} N_k & 0 & 0 & N_k\zeta\dfrac{h_k}{2}\bar{\mathbf{v}}_{1k}^x & -N_k\zeta\dfrac{h_k}{2}\bar{\mathbf{v}}_{2k}^x \\ 0 & N_k & 0 & N_k\zeta\dfrac{h_k}{2}\bar{\mathbf{v}}_{1k}^y & -N_k\zeta\dfrac{h_k}{2}\bar{\mathbf{v}}_{2k}^y \\ 0 & 0 & N_k & N_k\zeta\dfrac{h_k}{2}\bar{\mathbf{v}}_{1k}^z & -N_k\zeta\dfrac{h_k}{2}\bar{\mathbf{v}}_{2k}^z \end{bmatrix}. \tag{A2}$$